Nanoscale

PAPER

View Article Online
View Journal | View Issue

Cite this: *Nanoscale*, 2024, **16**, 5313

Merging gold plasmonic nanoparticles and L-proline inside a MOF for plasmon-induced visible light chiral organocatalysis at low temperature†

A. Kushnarenko,[a] A. Zabelina,[a] O. Guselnikova,[b] E. Miliutina,[a] B. Vokatá,[a] D. Zabelin,[a] V. Burtsev,[a] R. Valiev,[c] Z. Kolska,[d] M. Paidar,[e] V. Sykora,[f] P. Postnikov,*[b] V. Svorcik[a] and O. Lyutakov*[a]

Received 18th September 2023,
Accepted 22nd January 2024

DOI: 10.1039/d3nr04707e

rsc.li/nanoscale

Light-driven asymmetric photocatalysis represents a straightforward approach in modern organic chemistry. In comparison to the homogeneous one, heterogeneous asymmetric photocatalysis has the advantages of easy catalyst separation, recovery, and reuse, thus being cost- and time-effective. Here, we demonstrate how plasmon-active centers (gold nanoparticles – AuNPs) allow visible light triggering of chiral catalyst (proline) in model aldol reaction between acetone and benzaldehyde. The metal–organic framework UiO-66–NH_2 was used as an advanced host platform for the loading of proline and AuNPs and their stabilization in spatial proximity. Aldol reactions were carried out at a low temperature (–20 °C) under light illumination which resulted in 91% ee with a closed-to-quantitative yield, 4.5 times higher than that without light (*i.e.* in the absence of plasmon triggering). A set of control experiments and quantum chemical modeling revealed that the plasmon assistance proceeds through hot electron excitation followed by an interaction with an enamine with the formation of anion radical species. We also demonstrated the high stability of the proposed system in multiple catalytic cycles without leaching metal ions, which makes our approach especially promising for heterogeneous asymmetric photocatalysis.

Introduction

The preparation of enantiomerically pure compounds represents a key feature and challenge of advanced modern organic chemistry.[1,2] In this sense, enantioselective organocatalysis plays a central role, being considered a powerful tool, complementing organometallic and enzymatic catalysis.[3–6] The high degree of enantio-control, easiness of enantioselectivity prediction, functional group tolerance, and green conditions make the implementation of chiral catalysts an excellent approach.[6]

Light-driven processes as an option for enantioselective catalysis are advantageous due to the possibility of using clean, affordable and inexhaustible solar energy.[2,7] Nowadays, there are two main approaches for the design of photo-activated enantioselective catalysts: homogeneous and heterogeneous ones. The first one is connected with a combination of chiral auxiliary units with photoredox moieties (Ru, Ir, Rh, and Ni complexes) or organic photosensitive compounds[8,9] (see Fig. 1A). Irrespective of the high efficacy of homogeneous catalysts, considerable enantioselectivity, and desired product yields, the described catalytic systems have high complexity and require much synthetic efforts.[10,11]

The obvious complexity and high cost of common organic or organometallic catalysts forced the search for alternatives with higher industrial potential. Recently, semiconducting TiO_2 (or similar semiconductors) in the form of quantum dots (QDs) was reported to work in tandem with chiral molecules to give heterogeneous photocatalysts[2] (Fig. 1A). Heterogeneous catalysts are distinguished by easy separation, recovery, and reuse merits and in this respect they are cost- and time-effective.[2] However, the potential of TiO_2 and QDs is limited by their relatively low adsorption capacity, rapid electron–hole recombination and high aggregation tendency.[12] Despite the remarkable progress in heterogeneous chiral photocatalysts,

[a]*Department of Solid State Engineering, University of Chemistry and Technology, 16628 Prague, Czech Republic. E-mail: lyutakoo@vscht.cz*
[b]*Research School of Chemistry and Applied Biomedical Sciences, Tomsk Polytechnic University, Russian Federation. E-mail: postnikov@tpu.ru*
[c]*Kazan Federal University, 420008 Kazan, Russian Federation*
[d]*Centre for Nanomaterials and Biotechnology, J. E. Purkyne University, 40096 Usti nad Labem, Czech Republic*
[e]*Department of Inorganic Technology, University of Chemistry and Technology, 16628 Prague, Czech Republic*
[f]*Department of Water Technology and Environmental Engineering, University of Chemistry and Technology, 166 28 Prague, Czech Republic*
† Electronic supplementary information (ESI) available. See DOI: https://doi.org/10.1039/d3nr04707e

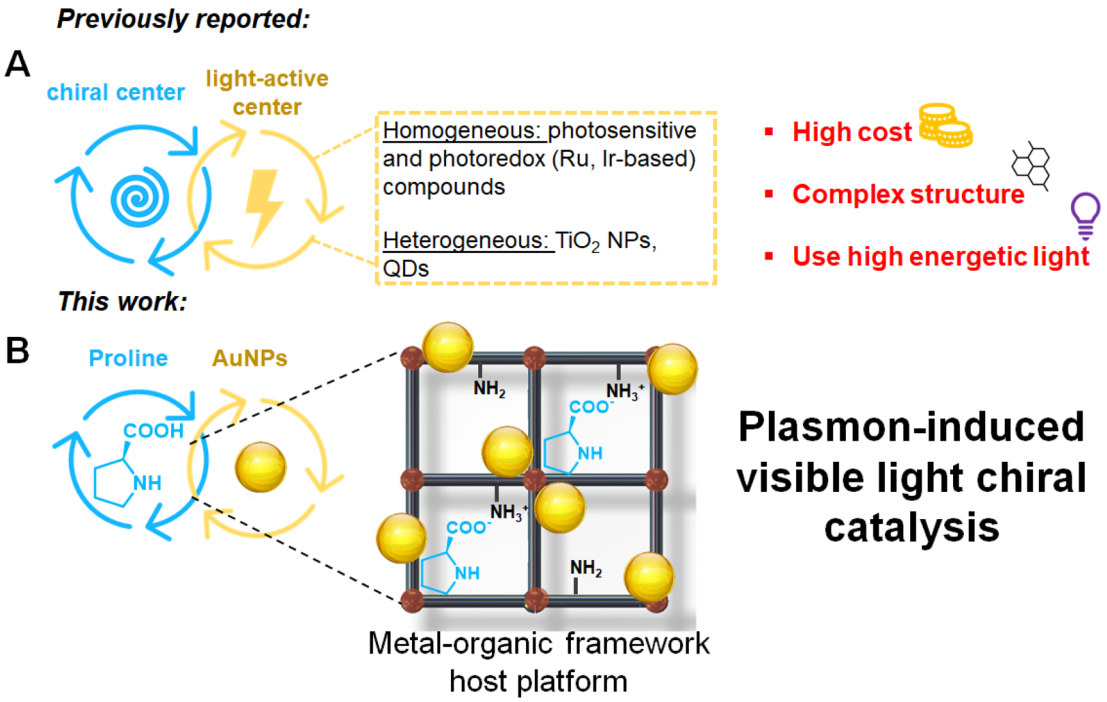

Fig. 1 (A) Typical chiral photocatalytic system based on chiral centers and plasmon active centers; (B) L-proline combined with plasmon active AuNPs inside a metal–organic framework host platform in this work.

the challenge in minimizing the participation of uncontrolled racemic background processes remains unchanged.[2] In heterogeneous photocatalysis, precise control of enantioselectivity is hampered by the intrinsic properties of the generated intermediate radicals and radical ions, such as high reactivity and low stability. Another challenge, associated with heterogeneous catalysts, is insufficient utilization of the (sun)light spectrum, since the used materials commonly absorb light only in the UV (or closed) spectral range.[2,12]

Absorption of the visible part of the sunlight spectrum can be ensured by the introduction of plasmon active nanostructures (NSs), which have already been used widely in plasmon assisted chemistry[12–15] (Fig. 1B). In this case, the chiral centers are coupled with plasmon-active NSs, which play a similar role as previously reported "light absorption" centers, providing charge carriers and ensuring excitation state transfer.[13–16] In addition, plasmon-assisted chemistry has been demonstrated to be effective at low temperature(s), which can positively affect the catalyst's stability and reaction enantioselectivity and prevents the reaction mixture contamination by metal ions from hetero-catalysts.[17,18]

Results and discussion

To take advantage of heterogeneous chiral photocatalysis, we chose a metal organic framework (MOF) as an advanced host platform because of its long-range ordered structure, highly accessible surface area, and easily achievable structure[19] (Fig. 1B). We combined UiO-66–NH_2 with gold nanoparticles (AuNPs) to ensure the close vicinity of the chiral catalyst (proline) and light-sensitizing AuNPs and achieve their effective cooperative work. For loading UiO-66–NH_2 with plasmon active AuNPs, a MOF was synthesized in the presence of AuNPs (a detailed description of the hybrid photocatalyst qualitative and quantitative optimization is described in the ESI – see Fig. S1† and related discussion). In this synthetic route, AuNPs can be entrapped by growing MOFs or serve as growth nucleation centres, resulting in the placement of AuNPs on the UiO-66–NH_2 surface or inside its pores. In both cases, a close contact between AuNPs and semiconductive UiO-66–NH_2 was achieved. In such a case, a scenario of the transfer of hot electron(s) to the conductive band of MOFs (or an excited energy state(s) with the excitation of the inner MOF electrons) can be realized, as was reported previously.[20]

Proline was chosen as a chiral catalyst because of its simple structure and relatively small molecular size suitable for loading into MOFs. The perfect combination of a secondary amine and a carboxylic acid makes it an efficient and versatile organocatalyst for a series of asymmetric catalytic processes, including the aldol reaction, the Mannich reaction, the Michael reaction, the Diels–Alder reaction, α-amination of aldehydes, and α-alkylation of aldehydes.[21,22] Au@UiO-66–NH_2 powder was loaded with proline *via* post-synthetic modification[23,24] by direct interaction of the MOF with the proline solution. The carboxylic groups of proline can protonate NH_2 groups with the formation of anilinium salt (Fig. 1B) to achieve a high degree of catalyst loading and maintain its

functionality (in particular by prevention of racemization).[23,25,26] After proline entrapping, the created material was further referred to as Au@UiO-66/proline.

The characterization of the structure of the optimized hybrid catalyst is presented in Fig. 2 and partially in the ESI (the optimization procedure is described in the ESI†). First, the XRD results (Fig. 2A) of separately prepared UiO-66–NH_2 and AuNPs@UiO-66–NH_2 indicate the presence of the main characteristic pattern of the metal organic framework and the Au pattern (in the case of AuNPs@UiO-66–NH_2), which correspond to the (111) and (200) crystalline phases. The presence of both AuNPs and the MOF is also evident through the characteristic peaks in the X-ray photoelectron spectroscopy (XPS) survey spectrum (as shown in Fig. 2B and listed in Table S1†). Despite the screening of the Au surface using the UiO-66–NH_2 layer, the intensity of the Au-related signal is still noticeable. The porosity of UiO-66–NH_2 and AuNPs@UiO-66–NH_2 was determined from the N_2 adsorption–desorption isotherms at 77 K (Table S2†). UiO-66–NH_2 shows typical microporosity with 820 m^2 g^{-1} surface area[27] and the synthesis of UiO-66–NH_2 in the presence of AuNPs produces a material with a similar surface area. Since the preparation route of Au@UiO-66–NH_2 is different from the common route (synthesis in the presence of NPs), its pore size distribution is different compared to that of pristine UiO-66–NH_2 or previously reported results (Fig. S2†).[19,28]

To confirm the successful loading of proline to materials, we performed FTIR analysis at each stage of preparation of Au@UiO-66–NH_2/proline. Loading of proline leads to the appearance of several additional vibration bands, evident from the FTIR spectra (Fig. 2C). The appearance of additional peaks in the 800–1200 cm^{-1} spectral region, as well as the widening (with a characteristic tooth appearance) of the initial narrow absorption peak of Au@UiO-66 located at 670, 1383, and

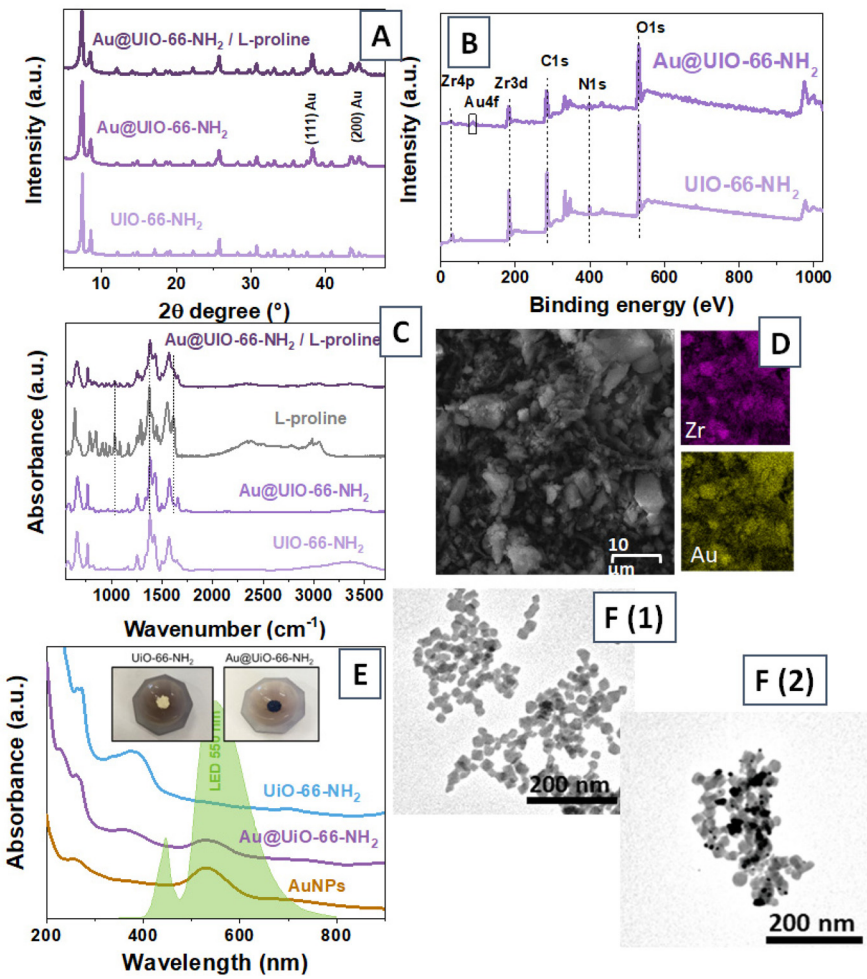

Fig. 2 Characterization of the catalyst structure: (A) XRD patterns of separately prepared UiO-66–NH_2 powder and Au@UiO-66–NH_2 powders before and after proline entrapping; (B) XPS survey spectra of UiO-66–NH_2 and Au@UiO-66–NH_2 powders; (C) FTIR absorption spectra of separately prepared UiO-66–NH_2, proline and Au@UiO-66–NH_2 powders before and after proline entrapping; (D) SEM-EDX characterization of Au@UiO-66–NH_2 (morphology and elemental composition); (E) UV-Vis spectra of Au@UiO-66–NH_2 dispersion and separately prepared AuNPs or UiO-66–NH_2 dispersions (the LED emission spectrum is also presented, the insert shows the photos of UiO-66–NH_2 and Au@UiO-66–NH_2 powders); (F) TEM images of UiO-66–NH_2 (F1) and Au@UiO-66–NH_2 (F2) samples.

1577 cm^{-1}, indicates the successful proline loading by Au@UiO-66.[29] Moreover, salt formation is proved by shifting of the N–H stretching vibration from 3476, 3557 cm^{-1} to 3468, 3353 cm^{-1} and broadening of the peak at 1434 cm^{-1} (symmetric COO^- stretching).[30] In addition, the total organic carbon (TOC) analysis of the supernatant solution after proline entrapping into Au@UiO-66–NH_2 shows <0.05 mg mL^{-1} concentration (Fig. S3† and related discussion). The extremely low TOC confirms the successful proline entrapping too. We also did not observe any XRD pattern from the proline powder (Fig. 2A *vs.* Fig. S4† – the absence of characteristic proline-related reflexes located at 15.2, 18.2, 19.6, 22.7, and 24.9 $2\theta^{\circ}$ is evident). This finding confirmed that proline formed a salt with the amino groups of the MOF. Proline loading into the accessible pores of Au@UiO-66–NH_2 leads to the suppression of the surface area and pore volume, which also confirms the successful proline entrapping (Fig. S2, Table S2†). As a result, we obtained an architecture, where ~ 40 nm AuNPs are located outside of the pores of UiO-66–NH_2, while proline as a small molecule is localized inside the pores. In this system, proline cannot interact directly with AuNPs; however, plasmonic metal/MOF heterostructures utilize the MOF substrate to capture the generated hot carriers on the MOF's conduction band and inject it to the reactant.[31]

The morphology of Au@UiO-66–NH_2 and that of separately prepared UiO-66–NH_2, (given for comparison) are presented in Fig. 2B and F. The *in situ* preparation of Au@UiO-66–NH_2 gives a relatively small MOF crystal size with an irregular morphology, where AuNPs are located at the same place as MOFs (Fig. 2F (1) *vs.* (2), – the TEM images of the pristine MOF and the MOF synthesized in the presence of AuNPs were compared). The corresponding SEM-EDX mappings also reveal a good spatial overlap of the characteristic Au and Zr signals, indicating that UiO-66–NH_2 is formed in close vicinity to AuNPs (Fig. 2D). Considering the synthetic route (MOF preparation in the presence of AuNPs), it can be expected that the nanoparticles are captured by the MOF or absorbed onto its surface. In both cases, the main goal was achieved – *i.e.* the spatial proximity of UiO-66–NH_2 (and proline) and AuNPs, which is a key factor in the plasmon triggering/activation of the MOF/proline system.

To probe the plasmonic activity of Au@UiO-66–NH_2/proline, we recorded UV-Vis spectra to estimate the wavelength position of plasmon absorption bands, which was found to be in the 500–600 nm range (Fig. 2E). As can be expected, the presence of AuNPs causes distinct changes in the color of the Au@UiO-66 powder (Fig. 2E – insert) when compared to pristine UiO-66–NH_2, due to the emergence of a characteristic plasmon absorption band. Thus, for all further experiments we used an LED with 550 nm (100 mW cm^{-2}) emission wavelength, which overlaps well with the plasmon absorption band of UiO-66@AuNPs/proline (the full LED emission spectrum is also presented in Fig. 2E). It should be noted that our system allows for the utilization of less energetic light compared to TiO_2-based catalysts commonly used for enantioselective transformations.[32,33] Moreover, the used wavelengths well overlap with the energy distribution maximum of the sunlight spectrum – the maximum of the solar energy flux belongs to photons with a wavelength(s) near 550 nm.

In the next step, we proceed with the utilization of Au@UiO-66–NH_2/proline for plasmon-assisted triggering of enantioselective catalysis (Fig. 3) performed at low temperature (except for several control cases). We used a model reaction of aldol condensation between 4-nitrobenzaldehyde and acetone at −20 °C.[34] Without light activation, the reaction proceeds at low temperature very slowly and only 20% conversion was

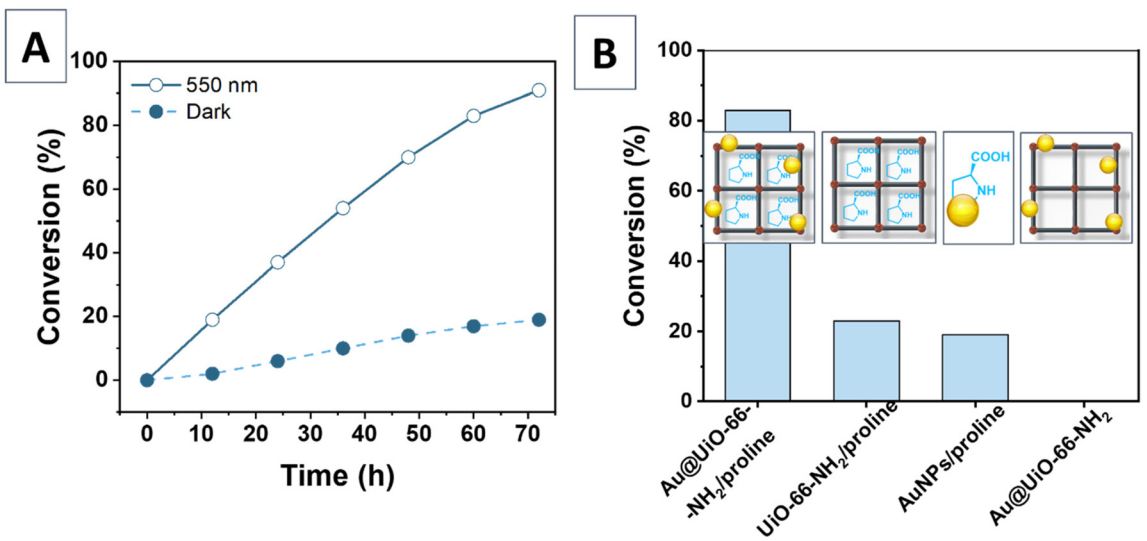

Fig. 3 (A) Time-resolved conversions of 4-nitrobenzaldehyde in aldol reactions with acetone; (B) control experiments: conversion of 4-nitrobenzaldehyde in the aldol reaction catalyzed by UiO-66–NH_2/proline (absence of AuNPs), AuNPs/proline (without UiO-66–NH_2, *i.e.* the absence of the spatial proximity of AuNPs and proline), and AuNPs@UiO-66–NH_2 (absence of proline).

achieved after 72 hours (Fig. 3A). The enantioselectivity (ee) of the aldol reaction without light was 93%, which is obviously connected with the low conversion. However, under illumination at 550 nm wavelength, the reaction is accelerated by a factor of about 4.5, confirming in this way the importance of plasmon active nanoparticles. In addition to the reaction enhancement, we also observed the ee conservation, which was found to be above 90%. Similar results were also obtained using 4-chlorobenzaldehyde, where a very slow reaction progress at low temperature (conversion below 20%) was significantly accelerated (conversion above 80%) under plasmon assistance. In addition, the proline-catalyzed aldol reaction of acetone and 4-chlorbenzaldehyde led to the formation of a thermally unstable 4-(4-chlorophenyl)-4-hydroxybutan-2-one, which tends to eliminate water with the formation of an undesired Mannich product.[35] In our case, the utilisation of plasmon assistance at low temperatures prevents such a process, and only a trace of the Mannich product has been observed (Fig. S5†). We also checked the ability to perform plasmon activation at low temperature for alternative substrates (Au@UiO-66–NH_2/proline-catalysed reaction between benzaldehyde and 2-butanon). Like in the previous case, the reaction was performed at low temperature (−20° C) with or without plasmon triggering. In both cases, we observed a significant enhancement of the reaction rate under plasmon assistance – Fig. S6† (without the formation of by-products, but with the loss of water molecules, unlike the previous case).

So, our systems overperform other catalytic systems based on MOFs and L-proline in terms of the balance between conversion, enantioselectivity and reaction time (Table 1 [36–40]). Au@UiO-66–NH_2/proline shows higher ee then L-proline itself and other proline-based catalysis systems based on polymers or graphene oxide.[4,41–43] It is therefore evident that compared to alternative approaches, the merging of plasmonics and chiral centers inside the host MOF allows us to achieve similar or even higher reaction yields, with improved enantioselectivity and the ability to prevent the formation of undesired products. It should also be noted that the reaction enantioselectivity was achieved through the utilisation of proline as a chiral auxirally agent. The low temperature of the reaction mixture allows for achieving a higher value of ee, but simultaneously leads to a lower reaction yield and an increase of required reaction time. To compensate for this drawback and to achieve both high reaction yield and high ee values, the non-thermal plasmon-based triggering of proline activity is proposed.

The importance of Au@UiO-66–NH_2/proline architecture is demonstrated by several control experiments performed under 550 nm light irradiation. Firstly, the key role of plasmon active centers is proven by the four-times decrease of conversion in the absence of light illumination and under light illumination of UiO-66–NH_2/proline but without the addition of AuNPs (Fig. 3B). The spatial proximity of AuNPs and proline was ensured by the porous nature of UiO-66–NH_2 itself. To check this notion, we performed a reaction using the Au/proline system, which also exhibits four-times lower conversion (in this case the AuNPs and MOFs are not situated in close vicinity and thus the electron or excited state transfer is not allowed or significantly restricted, leading to the "common" proline catalysis). In other word, the low efficiency is explained by the low probability of event, where AuNPs, the excited plasmon, proline and the substrate are met simultaneously to accomplish the reaction. Similarly, the absence of AuNPs in the reaction system (UiO-6–NH_2/proline case) also leads to the absence of plasmon triggering. As a result, the reaction is catalysed solely by "non-activated" proline and proceeds with a similar efficiency as in the previous case. As could also be expected, the complete absence of proline (Au@UiO-66–NH_2 utilization) leads to complete reaction interruption. Summarizing the results of control experiments allow us to conclude that: (i) the activation of AuNPs as light absorption centers and (ii) the proximity of plasmon active nanoparticles and chiral centers are quite critical for obtaining high conversion and ee.

The mechanism of the plasmonic reaction is still a very debatable question. Three dominant hypotheses are presently considered: (1) reactions are accelerated by plasmonic heating, (2) by transfer of hot carriers to the organic molecule followed by the formation of highly reactive species, or (3) by intramolecular excitation. To understand the mechanism of plasmonic asymmetric aldol condensation in our case, we first examined if plasmonic heating (plasmon-assisted light to heat conversion) contributes to the reaction. The direct measurements of reaction heating under light show that the reaction mixture was slightly heated by 4 °C after 72 hours of treatment

Table 1 Comparative results of proline-based catalysis: conditions, conversion, yield and ee

Catalyst	Substrate	Conditions	Yield	ee	Ref.
Metalloporphyrinc framework loaded with proline	Acetone	HBF_4, H_2O, DMF, 4 days	82	29	36
L-Proline-modulated UiO-66	Cyclohexanone	Methanol, 1 day	95	70	37
Zn-MOF-1 covalently coupled with L-proline	Cyclohexanone	Water, 7 days	75	70	38
IRMOF-pro covalently coupled with L-proline	Acetone	4 days	100	52	39
Cr-MIL-101 with polymerized proline[a]	Cyclohexanone	3 days	63	87	40
L-Proline	Acetone	1 day	68	76	4
Polystyrene derivatives carrying L-proline	Acetone	2 days	69	28	41
L-Proline/GO	Acetone	6 h	95	68	42
Hyperbranched polyethylene (HBPE)-supported L-proline[a]	Cyclohexanone	1 day	94	88	43
Au@UiO-66–NH_2/proline	Acetone	550 nm, 3 days	81	91	This work

[a] 4-Chlorobenzaldehyde.

(Fig. S7†). One can argue that the local heating (in place of plasmonic hot spots) can reach a significantly higher value, but in our case a continual light source with a moderate power density value of 100 mW cm^{-2} was used, which excludes significant catalyst heating (unlike, for example, utilisation of femto- or nano-pulsed laser sources[44,45]). In the control experiment, the LED power was varied from 0 to 175 mW cm^{-2} and a highly linear dependence of temperature on the power with R^2_{lin} = 0.99 was observed (see Fig. S8†). These data which lead us to discard the thermal effect and suggest that electron-based or intramolecular excitation processes are dominant in the plasmon triggering of proline-catalyzed aldol addition.[46,47]

In general, the enantioselectivity in proline catalysis of the aldol reaction is attributed to the rate-determining step of the C–C bond formation, which involves the nucleophilic addition of the previously formed enamine to the electrophilic aldehyde.[48] The ee of the resulted product in the reaction is closely related to the energy difference between the formed transition states.[49] On the other hand, at lower temperature, the energy is not enough to overcome the reaction barrier. At this stage, plasmon triggering can promote the activation of the generated enamine through the injection of hot electrons (*i.e.* increase of enamine nucleophilicity), facilitating the nucleophilic attack (Fig. 4A).[50,51] Alternatively, the plasmon-related high electric field can facilitate the C–C bond formation through intramolecular electron excitation of the enamine (Fig. 4B).

Taking into account the proposed reaction pathways, we carried out quantum chemical modeling by the time-dependent density functional theory[52] with the B3LYP[53] functional and the 6-31G(d,p) basis set for the proline excited states taking into account the interaction with hot electrons (Fig. 4A) and the intramolecular excitation (Fig. 4B) (the computational details are provided in the ESI†). The CAM-B3LYP functional was chosen since it works better than the common B3LYP functional (for the excited electronic state when an electronic transition has the charge transfer character[54,55]). The CAM-B3LYP functional contains from 19% non-local exchange in the short-range limit to 65% non-local exchange in the long-range limit. Therefore, it gives a better description of the charge transfer electronic transition, but usually the energy and oscillator strength of the excited electronic state are overestimated for a typical electronic transition without the charge transfer mixture. In our case, we deal with the electronic transition without the large charge transfer mixture where B3LYP works well for the TDDFT level of theory.

The intramolecular excitation of proline requires sufficient amount of energy for overcoming the energy gap ($S_0 \rightarrow S_1$ 4.8 eV), which sufficiently surpass a photon energy of 2.25 eV (Fig. 4B). Indeed, the energy gap of proline can be sufficiently decreased due to hybridization with the gold surface, as was reported earlier.[56] Nevertheless, in our case, proline is localized on the walls of UiO-66–NH_2 inside the pores (Fig. 1B) and cannot directly interact with the gold surface. Moreover, in our control experiments we did not observe the sufficient formation of products in the reaction catalyzed by the Au NPs/proline mixture (Fig. 3B). The final argument against the direct excitation mechanism is the behavior of the S_1 excited state (Fig. 4B), which is able to spontaneously decompose with the elimination of CO_2. Such a pathway should lead to the termination of the catalytic cycle, which has not been observed in our experiments. Thus, in view of the abovementioned experimental and theoretical results, we can dismiss the direct excitation as the main mechanism.

The hot electron transfer seems to be more favorable for the nucleophilic substitution due to the increase of electron density on the reacting enamine (Fig. 4C). First, L-proline inside the pores of UiO-66–NH_2@Au leads to the formation of

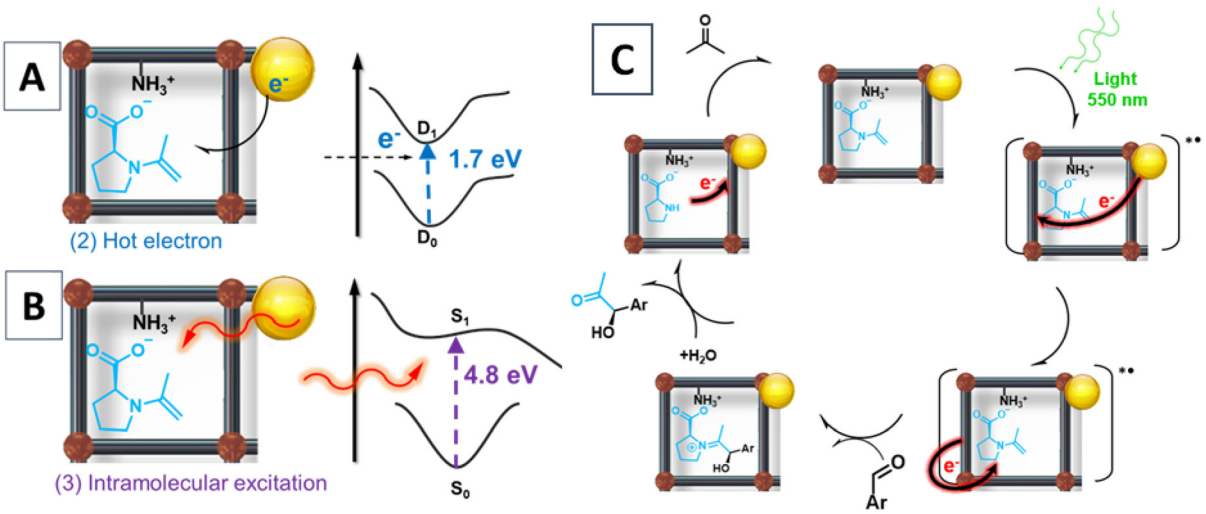

Fig. 4 Quantum chemical evaluation of the aldol reaction: (A) reaction profile for the hot electron pathway; (B) reaction profile for intramolecular HOMO–LUMO electron excitation; and (C) plausible mechanism of reaction proceeding revealed based on DFT calculations and control experiments.

an enamine, which is activated by injection of hot electrons with the formation of anion radical species, which can be excited by plasmons. This step could proceed directly due to the vicinity of enamine and AuNPs or thanks to UiO-66–NH_2 serving as a support for the hot electron transfer pathway (UiO-66–NH_2).[57] The energy gap in this case was 1.7 eV, which is well the below the photon energy. It should also be noted that the conduction band of the UiO-66–NH_2 MOF is 0.39 eV[58] and is significantly lower than the energy of incoming photons, thus the transfer of hot electrons from AuNPs to the MOF is also very likely. Moreover, the generated excited state D_1 is not dissociative. Thus, the increased nucleophilicity and relative stability of the anion radical excited state make possible the further interaction with aldehyde and continuation of the catalytic cycle (Fig. 4C).

Finally, we performed a few control experiments with the aim to confirm the hot electron-based reaction pathway in an experimental way. First, TEMPO (2,2,6,6-tetramethylpiperidinyloxy or 2,2,6,6-tetramethylpiperidine 1-oxyl) was added to the reaction solution as a hot electron scavenger. In this case, we observed some decrease of the conversion of 4-nitrobenzaldehyde with the concentration of added TEMPO (Fig. S9†). Obviously, the TEMPO molecules consume some of the plasmon-excited hot electrons and lead to reaction deceleration in this way. As an alternative control, Ag^+ salts were added to Au@UiO-66/proline suspension in methanol, leading to hot electron-induced silver reduction with the formation of insoluble Ag^0 (holes are used in methanol oxidation). The solid reaction residue was subsequently separated and subjected to SEM-EDX analysis. The results indicate the presence of Ag in the case of plasmon triggering in contrast to the control dark case (Fig. S10† and corresponding Table S3†). Therefore, the plasmon triggering can really excite hot electrons, participating in the above chemical reaction. Thus, both control experiments are in accord with the results of the DFT calculation.

Previously reported MOF/proline systems commonly lead to a gradual decrease in conversion and enantioselectivity after the first three cycles.[26,37,59–64] In our case, the drop in reaction yield and ee did not exceed 10% of the initial values even after 5 cycles of Au@UiO-66/proline utilization (Fig. 5A), as a result of relatively mild reaction conditions. For comparison, Fig. S11† shows the results achieved with Au@UiO-66–NH_2/proline utilization at RT (under plasmon triggering). As is evident, a noticeable worsening of catalyst efficiency was observed in this case compared to the lower temperature case. In turn, the leaching test (performed at −20 °C) showed that after the separation of Au@UiO-66–NH_2/proline from the reaction mixture by cold filtration, the reaction did not proceed (Fig. 5B). Similar reaction deceleration occurred when light illumination is turned off, confirming in this way the key role of plasmon active nanoparticles. Finally, we evaluated the stability of Au@UiO-66–NH_2/proline, since the residual concentration of metals in the reaction mixture[22,37,59–64] is a critical factor, especially under the reaction proceeding at RT with the utilization of two metals in the reaction mixture (Zr from UiO-66–NH_2 and Au from plasmon active AuNPs). However, in our case the reaction was performed at lower temperature and the residual metal concentrations determined using ICP-OES were just 0.5 μg L^{-1} of Zr and 7 μg L^{-1} (3.6 nM) of Au, which is considered to be relatively safe to living systems.[65,66] For comparison, the reaction proceeding at RT results in significantly higher metal ion leaching as demonstrated in Fig. S12.†

We believe that the proposed plasmon-active catalytic system can be successfully applied for a variety of reactions such as the preparation of heterocycles, α-aminoxylation as well as asymmetric Mannich and Michael reactions.[67–69] In such cases, the high efficiency and selectivity of the catalytic system as well as the activation by visible light will open a new avenue for the development of synthetic methods for fine organic synthesis.

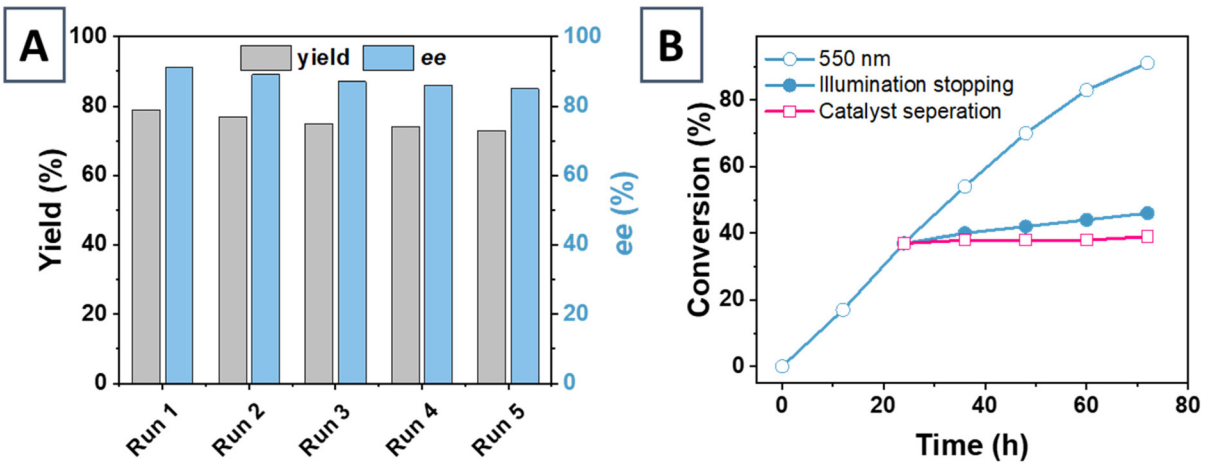

Fig. 5 (A) Yields and ee values of 4-hydroxy-4-(4-nitrophenyl)butan-2-one (−20 °C, plasmon triggering, 72 h.) in the several subsequent cycles of Au@UiO-66 utilization; (B) impact of catalyst leaching and illumination stopping on 4-nitrobenzaldehyde conversion under plasmon triggering at −20 °C.

Conclusions

In summary, we reported a versatile plasmon active heterogeneous platform for asymmetric organic photocatalysis – a model aldol reaction. Compared to previous reports that used inorganic semiconductors absorbing highly energetic light,[2] the use of stable AuNPs allows us to utilize visible light conversion to a chemical reaction. AuNPs as a plasmon active center and proline as a chiral center were loaded into UiO-66–NH_2, which appears to be a perfect platform for AuNP stabilization and easy experimental handling. The reaction was performed at a low temperature (−20 °C) and the synergy between photon absorption/plasmon excitation, charge separation, and chiral catalysis allows the successful aldol reaction with quantitative yields and enantioselectivity overperforming other catalytic systems based on MOFs and L-proline in terms of the balance between conversion, enantioselectivity and reaction time. We also demonstrated the sustainability of the proposed system, in particular – efficiency conservation (in terms of yield and ee) during the several subsequent runs of Au@UiO-66–NH_2/proline utilization as well as insignificant metal ion leaching in the reaction mixture. Apart from the advantageous performance, we probed three most common reaction pathways by a set of control experiments and quantum chemical modeling to shed light on the mechanism of light-induced asymmetric catalysis. We found that hot electrons interact with an enamine with the formation of anion radical species with an energy of 1.7 eV, which is well below the photon energy. The better understanding of the heterogeneous asymmetric photocatalysis mechanisms can facilitate the design and application of more efficient asymmetric photocatalytic systems.

Methods

Detailed description of used materials, sample preparation and measurement techniques is given in the ESI.† Briefly, gold nanoparticles (AuNPs) were prepared using the standard Turkevich method. Subsequently, UIO-66–NH_2 was synthesised in the presence of AuNPs using the solvothermal method. In several control cases, AgNPs were used instead of AuNPs or UIO-66–NH_2 synthesis was performed in the absence of metal nanoparticles. For proline entrapping, 5 g of Au@UIO-66–NH_2 (or UIO-66–NH_2 in the control experiments) were added to 10 mL of proline solution (0.5 mM) in acetone and gently stirred for 3 hours. The Me@UIO-66–NH_2 powders with entrapped proline molecules were separated by centrifugation and dried under vacuum. The entrapping of proline molecules was confirmed by total organic carbon (TOC) content analysis in the supernatant after evaporation, drying and re-dissolving in Milli-Q water.

26 mg of Au@UIO-66–NH_2/proline powder was dispersed in a solution of 4-chlorobenzaldehyde or 4-nitrobenzaldehyde (0.1 mmol, 2 mL acetone, 0.5 mL chloroform). Aldol reactions were carried out at −20 °C under illumination with an LED light source (550 nm central emission wavelength, Thorlabs, irradiance on the first glass surface – 100 mW cm^{-2}). In control experiments, reactions were carried out in the dark and/or at RT. The structure and purity of the reaction products were analyzed by GC-MS and NMR analyses.

The reaction conversion, yield, and enantiomeric excess were also determined by GC with a capillary chiral column (β-DEX™ 120 chiral capillary column, L × I.D. 30 × 0.25 mm^2, df 0.25 μm, Supelco) using racemic 4-hydroxy-4-(4-nitrophenyl) butan-2-one as a standard. To calculate the conversion, the calibration curve was obtained using 5 solutions with different concentrations of reactants (40, 20, 10, 5 and 2.5 mM).

Conflicts of interest

There are no conflicts to declare.

Acknowledgements

This work was supported by GACR under the project 23-08509S and the Russian Science Foundation (project no 23-73-00117) (the design of catalysts and reactivity studies). The quantum-chemical modeling was supported in part by the Kazan Federal University Strategic Academic Leadership Program ("PRIORITY2030").

References

1 J. Matsuo and M. Murakami, *Angew. Chem., Int. Ed.*, 2013, **52**, 9109–9118.
2 X. Qiu, Y. Zhang, Y. Zhu, C. Long, L. Su, S. Liu and Z. Tang, *Adv. Mater.*, 2021, **33**, 2001731.
3 M. T. Reetz, F. Kunisch and P. Heitmann, *Tetrahedron Lett.*, 1986, **27**, 4721–4724.
4 B. List, R. A. Lerner and C. F. Barbas, *J. Am. Chem. Soc.*, 2000, **122**, 2395–2396.
5 K. A. Ahrendt, C. J. Borths and D. W. C. MacMillan, *J. Am. Chem. Soc.*, 2000, **122**, 4243–4244.
6 B. Han, X.-H. He, Y.-Q. Liu, G. He, C. Peng and J.-L. Li, *Chem. Soc. Rev.*, 2021, **50**, 1522–1586.
7 W. Yao, E. A. Bazan-Bergamino and M.-Y. Ngai, *ChemCatChem*, 2022, **14**, e202101292.
8 D. Trauner, *Angew. Chem., Int. Ed.*, 2009, **48**, 6589–6589.
9 M. J. Genzink, J. B. Kidd, W. B. Swords and T. P. Yoon, *Chem. Rev.*, 2022, **122**, 1654–1716.
10 A. Tröster, R. Alonso, A. Bauer and T. Bach, *J. Am. Chem. Soc.*, 2016, **138**, 7808–7811.
11 R. Brimioulle, A. Bauer and T. Bach, *J. Am. Chem. Soc.*, 2015, **137**, 5170–5176.
12 Z. Zhang, C. Zhang, H. Zheng and H. Xu, *Acc. Chem. Res.*, 2019, **52**, 2506–2515.
13 E. Cortés, *Adv. Opt. Mater.*, 2017, **5**, 1700191.
14 O. Guselnikova, S. R. A. Marque, E. V. Tretyakov, D. Mares, V. Jerabek, G. Audran, J.-P. Joly, M. Trusova, V. Svorcik,

O. Lyutakov and P. Postnikov, *J. Mater. Chem. A*, 2019, **7**, 12414–12419.
15 O. Guselnikova, P. Postnikov, M. M. Chehimi, Y. Kalachyovaa, V. Svorcik and O. Lyutakov, *Langmuir*, 2019, **35**, 2023–2032.
16 O. Guselnikova, A. Olshtrem, Y. Kalachyova, I. Panov, P. Postnikov, V. Svorcik and O. Lyutakov, *J. Phys. Chem. C*, 2018, **122**, 26613–26622.
17 A. Zabelina, J. Dedek, O. Guselnikova, D. Zabelin, A. Trelin, E. Miliutina, Z. Kolska, J. Siegel, V. Svorcik, J. Vana and O. Lyutakov, *ACS Catal.*, 2023, **13**, 3830–3840.
18 O. Guselnikova, J. Váňa, L. T. Phuong, I. Panov, L. Rulíšek, A. Trelin, P. Postnikov, V. Švorčík, E. Andris and O. Lyutakov, *Chem. Sci.*, 2021, **12**, 5591–5598.
19 O. Semyonov, D. Kogolev, G. Mamontov, E. Kolobova, A. Trelin, M. S. Yusubov, O. Guselnikova and P. S. Postnikov, *J. Chem. Eng.*, 2022, **431**, 133450.
20 C. S. L. Koh, H. Y. F. Sim, S. X. Leong, S. K. Boong, C. Chong and X. Y. Ling, *ACS Mater. Lett.*, 2021, **3**, 557–573.
21 D. W. C. MacMillan, *Nature*, 2008, **455**, 304–308.
22 M. Zhou, E.-S. M. El-Sayed, Z. Ju, W. Wang and D. Yuan, *Inorg. Chem. Front.*, 2020, **7**, 1319–1333.
23 L. Cheng, K. Zhao, Q. Zhang, Y. Li, Q. Zhai, J. Chen and Y. Lou, *Inorg. Chem.*, 2020, **59**, 7991–8001.
24 J. Kimling, M. Maier, B. Okenve, V. Kotaidis, H. Ballot and A. Plech, *J. Phys. Chem. B*, 2006, **110**, 15700–15707.
25 C. Kutzscher, H. C. Hoffmann, S. Krause, U. Stoeck, I. Senkovska, E. Brunner and S. Kaskel, *Inorg. Chem.*, 2015, **54**, 1003–1009.
26 A. Gheorghe, B. Strudwick, D. M. Dawson, S. E. Ashbrook, S. Woutersen, D. Dubbeldam and S. Tanase, *Chem. – Eur. J.*, 2020, **26**, 13957–13965.
27 C. L. Luu, T. T. V. Nguyen, T. Nguyen and T. C. Hoang, *Adv. Nat. Sci.: Nanosci. Nanotechnol.*, 2015, **6**, 025004.
28 L. Chen, H. Chen, R. Luque and Y. Li, *Chem. Sci.*, 2014, **5**, 3708–3714.
29 R. Bhuvaneswari, S. Karthikeyan, S. Selvasekarapandian, D. Vinoth Pandi, N. Vijaya, A. Araichimani and C. Sanjeeviraja, *Ionics*, 2015, **21**, 387–399.
30 G. Socrates, *Infrared and Raman characteristic group frequencies: tables and charts*, John Wiley & Sons, 2004.
31 S. Wang, D. Tang, Y. Zhang and J. Zhao, *ChemPhysChem*, 2023, **24**, e202200565.
32 M. Mifsud, S. Gargiulo, S. Iborra, I. W. C. E. Arends, F. Hollmann and A. Corma, *Nat. Commun.*, 2014, **5**, 3145.
33 X.-H. Ho, M.-J. Kang, S.-J. Kim, E. D. Park and H.-Y. Jang, *Catal. Sci. Technol.*, 2011, **1**, 923–926.
34 S. Mandal, S. Mandal, S. K. Ghosh, A. Ghosh, R. Saha, S. Banerjee and B. Saha, *Synth. Commun.*, 2016, **46**, 1327–1342.
35 C. Han, S.-H. Li, Z.-R. Tang and Y.-J. Xu, *Chem. Sci.*, 2018, **9**, 8914–8922.
36 W.-L. He, M. Zhao and C.-D. Wu, *Angew. Chem., Int. Ed.*, 2019, **58**, 168–172.
37 X. Feng, H. S. Jena, K. Leus, G. Wang, J. Ouwehand and P. Van Der Voort, *J. Catal.*, 2018, **365**, 36–42.
38 W. Zhu, C. He, P. Wu, X. Wu and C. Duan, *Dalton Trans.*, 2012, **41**, 3072–3077.
39 D. J. Lun, G. I. N. Waterhouse and S. G. Telfer, *J. Am. Chem. Soc.*, 2011, **133**, 5806–5809.
40 X.-W. Dong, Y. Yang, J.-X. Che, J. Zuo, X.-H. Li, L. Gao, Y.-Z. Hu and X.-Y. Liu, *Green Chem.*, 2018, **20**, 4085–4093.
41 A. Ikeda, K. Terada, M. Shiotsuki and F. Sanda, *J. Polym. Sci., Part A: Polym. Chem.*, 2011, **49**, 3783–3796.
42 R. Tan, C. Li, J. Luo, Y. Kong, W. Zheng and D. Yin, *J. Catal.*, 2013, **298**, 138–147.
43 S. Wang, P. Liu, W. J. Wang, Z. Zhang and B. G. Li, *Catal. Sci. Technol.*, 2015, **5**, 3798–3805.
44 S. Hashimoto, D. Werner and T. Uwada, *J. Photochem. Photobiol.*, 2012, **13**, 28–54.
45 M. Nazemi, S. R. Panikkanvalappil, C.-K. Liao, M. A. Mahmoud and M. A. El-Sayed, *ACS Nano*, 2021, **15**, 10241–10252.
46 G. Baffou, I. Bordacchini, A. Baldi and R. Quidant, *Light: Sci. Appl.*, 2020, **9**, 108.
47 E. Miliutina, O. Guselnikova, P. Bainova, Y. Kalachyova, R. Elashnikov, M. S. Yusubov, V. V. Zhdankin, P. Postnikov, V. Švorčík and O. Lyutakov, *Adv. Mater. Interfaces*, 2018, **5**, 1800725.
48 S. Bahmanyar, K. N. Houk, H. J. Martin and B. List, *J. Am. Chem. Soc.*, 2003, **125**, 2475–2479.
49 C. Allemann, R. Gordillo, F. R. Clemente, P. H.-Y. Cheong and K. N. Houk, *Acc. Chem. Res.*, 2004, **37**, 558–569.
50 H. Li, F. Qin, Z. Yang, X. Cui, J. Wang and L. Zhang, *J. Am. Chem. Soc.*, 2017, **139**, 3513–3521.
51 L. Huang, J. Zou, J.-Y. Ye, Z.-Y. Zhou, Z. Lin, X. Kang, P. K. Jain and S. Chen, *Angew. Chem., Int. Ed.*, 2019, **58**, 8794–8798.
52 M. E. Casida, in *Recent Advances in Density Functional Methods*, World scientific, 1995, vol. 1, pp. 155–192.
53 C. Lee, W. Yang and R. G. Parr, *Phys. Rev. B: Condens. Matter Mater. Phys.*, 1988, **37**, 785–789.
54 H. S. Mosher, M. B. Frankel and M. Gregory, *J. Am. Chem. Soc.*, 1953, **75**, 5326–5328.
55 D. J. Tozer, *J. Chem. Phys.*, 2003, **119**, 12697–12699.
56 D. Votkina, P. Petunin, E. Miliutina, A. Trelin, O. Lyutakov, V. Svorcik, G. Audran, J. Havot, R. Valiev, L. I. Valiulina, J.-P. Joly, Y. Yamauchi, J. H. Mokkath, J. Henzie, O. Guselnikova, S. R. A. Marque and P. Postnikov, *ACS Catal.*, 2023, **13**, 2822–2833.
57 C. S. L. Koh, H. Y. F. Sim, S. X. Leong, S. K. Boong, C. Chong and X. Y. Ling, *ACS Mater. Lett.*, 2021, **3**, 557–573.
58 K. Gayathri, K. Vinothkumar, Y. N. Teja, B. M. Al-Shehri, M. Selvaraj, M. Sakar and R. Balakrishna, *Colloids Surf., A*, 2022, **653**, 129992.
59 J. Zhu, X. Meng, W. Liu, Y. Qi, S. Jin and S. Huo, *RSC Adv.*, 2022, **12**, 21574–21581.
60 L. Lili, Z. Xin, R. Shumin, Y. Ying, D. Xiaoping, G. Jinsen, X. Chunming and H. Jing, *RSC Adv.*, 2014, **4**, 13093–13107.

61 L. Cheng, Q. Guo, K. Zhao, Y.-M. Li, H. Ren, C.-Y. Ji and W. Li, *Catal. Lett.*, 2023, **153**, 1024–1035.
62 D. Wu, J. Chen, D. Tu, Y. Zhuang and L. Shen, *Inorg. Chem. Commun.*, 2020, **119**, 108052.
63 M. Mutiah, S. Rochat, I. Amura, A. D. Burrows and E. A. C. Emanuelsson, *Chem. Eng. Process.*, 2021, **161**, 108315.
64 K. D. Nguyen, C. Kutzscher, S. Ehrling, I. Senkovska, V. Bon, M. de Oliveira, T. Gutmann, G. Buntkowsky and S. Kaskel, *J. Catal.*, 2019, **377**, 41–50.
65 A. M. Alkilany and C. J. Murphy, *J. Nanopart. Res.*, 2010, **12**, 2313–2333.
66 J. A. Khan, B. Pillai, T. K. Das, Y. Singh and S. Maiti, *ChemBioChem*, 2007, **8**, 1237–1240.
67 B. S. Vachan, M. Karuppasamy, P. Vinoth, S. Vivek Kumar, S. Perumal, V. Sridharan and J. C. Menéndez, *Adv. Synth. Catal.*, 2020, **362**, 87–110.
68 P. Kumar and N. Dwivedi, *Acc. Chem. Res.*, 2013, **46**, 289–299.
69 J. Liu and L. Wang, *Synthesis*, 2017, **49**, 960–972.